

Three-dimensional Hydrodynamic Simulations of the Combustion of a Neutron Star into a Quark Star

Matthias Herzog

*Max-Planck-Institut für Astrophysik, Karl-Schwarzschild-Str. 1, D-85741 Garching, Germany**

Friedrich K. Röpke

*Institut für Theoretische Physik und Astrophysik, Universität Würzburg,
Emil-Fischer-Str. 31, D-97074 Würzburg, Germany*

(Dated: December 28, 2021)

We present three-dimensional numerical simulations of turbulent combustion converting a neutron star into a quark star. Hadronic matter, described by a micro-physical finite-temperature equation of state, is converted into strange quark matter. We assume this phase, represented by a bag-model equation of state, to be absolutely stable. Following the example of thermonuclear burning in white dwarfs leading to Type Ia supernovae, we treat the conversion process as a potentially turbulent deflagration. Solving the non-relativistic Euler equations using established numerical methods we conduct large eddy simulations including an elaborate subgrid scale model, while the propagation of the conversion front is modeled with a level-set method. Our results show that for large parts of the parameter space the conversion becomes turbulent and therefore significantly faster than in the laminar case. Despite assuming absolutely stable strange quark matter, in our hydrodynamic approximation an outer layer remains in the hadronic phase, because the conversion front stops when it reaches conditions under which the combustion is no longer exothermic.

I. INTRODUCTION

Based on earlier work by Bodmer [1] and Itoh [2], Witten [3] suggested that a mixture of about the same number of u-, d- and s-quarks, called strange quark matter (SQM), was the true ground state of matter, whereas ordinary nuclear matter is only a metastable, yet usually extremely long-lived state. This conjecture, known today as *strange matter hypothesis*, was discussed lively ever since, but no final verdict about its correctness could be made because the equation of state (EoS) of cold dense matter is still largely unknown. Matter in this extreme state is inaccessible to laboratory experiments; compact stars, however, offer a possibility to test the strange matter hypothesis. Shortly after Witten's work also Haensel et al. [4] and Alcock et al. [5] proposed *strange stars*, compact stars consisting entirely of SQM. Alcock et al. [5] based their work on the idea that compact stars are not born as strange stars, but as hadronic neutron stars, which later are converted into strange stars or *hybrid stars* – compact stars consisting of a quark core and hadronic outer layers.

Hadronic matter does not decay into SQM spontaneously, even though it would be energetically favorable, because this process would require a large amount of simultaneous weak reactions – the probability for this to happen is vanishingly low. But if some SQM already exists inside a neutron star, the diffusion of s-quarks from this seed into the surrounding hadronic matter would convert it into SQM. This conversion process should take place in a confined region and on length-scales small compared to the size of the star. It is expected to occur

only if the conversion releases energy, that is, if it is an exothermic process. The described situation is therefore similar to the propagation of a chemical flame, or even more similar to the thermonuclear burning inside a white dwarf during a Type Ia supernova (SN Ia). Thus, it is natural to think of the conversion of hadronic matter into SQM as a “combustion”. In the spirit of this analogy, we will sometimes refer to the conversion as “burning” and to the conversion front as “flame front”. Alcock et al. [5] were the first to suggest that a strange star may originate from a combustion of an ordinary neutron star. They also considered how a SQM seed which subsequently triggers the conversion into a strange star may come about and described various possibilities by either internal nucleation or external seeding. Subsequently the idea of a combustion was discussed in more detail by various authors [6–13].

The laminar conversion velocity was first estimated by Olinto [14], and, with similar results, by Heiselberg et al. [15]. Based on their results, Olesen and Madsen [7] calculated the burning of a neutron star using a one-dimensional model with laminar burning and obtained conversion timescales from 10^{-1} s to 10^2 s. Horvath and Benvenuto [6] suggested that the combustion should be turbulent due to various instabilities of the conversion front and therefore the conversion velocity should be enhanced considerably (see [16] for a recent update). Lugones et al. [9] and Lugones and Benvenuto [10] pointed out the importance of the conditions for an exothermic combustion. The combustion mode was discussed from a hydrodynamic point of view also by Cho et al. [8], Tokareva and Nusser [11] and Drago et al. [12], where the latter expected the burning to be subsonic, although accelerated by turbulence. New ideas concerning the initial seeding were recently published by Perez-Garcia et al.

* mherzog@mpa-garching.mpg.de

[17]. They suggested that the self-annihilation of weakly interacting dark matter particles (WIMPs) inside a neutron star may provide a SQM seed. Recently, hydrodynamic simulations of the combustion front were presented by Niebergal et al. [13]. Their results of the laminar conversion velocity differed strongly from earlier estimates. On the observational side Leahy and Ouyed [18], extended in Ouyed et al. [19], examined the supernova SN 2006gy and suggested that this extremely luminous event can be explained by a “quark nova” – the transition of the newly formed neutron star to a strange quark star shortly after a core collapse supernova of a very massive star.

Here we study the dynamical behavior of the conversion inside a neutron star. We model the conversion as a combustion, particularly as a subsonic deflagration. As mentioned above, it is widely assumed that the conversion process turns turbulent [e.g. 6, 12, 16], but dynamical, multi-dimensional simulations have never been performed. Thus, our main focus will be to explore if and how turbulent motion occurs during the conversion process and to which consequences for the final state of the neutron star this may lead.

This work is organized as follows: In Section II we describe the EoS that we use in our calculations. In Section III we introduce our concept of modeling the conversion as a turbulent combustion, and in Section IV our numerical method is explained. We present numerical simulations and their results in Section V and conclude in Section VI.

II. EQUATION OF STATE

A. Equation of State for Hadronic Matter

We consider the two micro-physical, finite temperature EoS which are most frequently used in simulations of astrophysical events such as core collapse supernovae and neutron star mergers: the EoS by Lattimer and Swesty [20] (LS EoS) and by Shen et al. [21] (Shen EoS). The LS EoS is based on a non-relativistic liquid drop model with an incompressibility modulus of $K = 180$ MeV. For calculating the Shen EoS relativistic mean field theory was applied, here $K = 280$ MeV is adopted.

The recent measurement of the Shapiro delay of the binary millisecond pulsar J1614-2230 [22] yields a gravitational mass of the pulsar of $M = (1.97 \pm 0.04) M_\odot$. In contrast to the Shen EoS, the LS EoS is rather soft. Consequently it leads to a maximum mass for a hadronic non-rotating neutron star of only $M_{\text{max}}^{\text{LS}} \sim 1.8 M_\odot$ and is therefore in conflict with the observation of pulsar J1614-2230. We nevertheless use the LS EoS in this work, because we do not claim to conduct realistic simulations but we rather see our work as a first step into this so far mostly unexplored field. An alternative would be to change the incompressibility modulus of the LS EoS to $K = 220$ MeV, which leads to a maximum mass com-

patible with the observations. We discuss this possibility briefly in Section III B.

For simplicity we assume for all our calculations a constant low proton fraction Y_p . Variations of its value, particularly assuming β -equilibrium, do not lead to a significant change of our results, as is shown exemplary in Section III B. In the same section we explain that for physical reasons it turned out that it was impossible to use the Shen EoS, thus we perform all our simulations using the LS EoS.

B. Equation of State for Strange Quark Matter

We describe SQM by a simple bag model for finite temperatures [23] based on the MIT bag model [24]. This model treats SQM as ideal Fermi gases of massless and non-interacting u-, d-, and s-quarks inside a confining bag. Since in this approximation the quarks can be described by only one chemical potential, the resulting analytic expressions for pressure P , energy density e and baryon number density n as function of the bag constant B and the chemical potential μ are [11, 25]

$$P = \frac{19}{36}\pi^2 T^4 + \frac{3}{2}T^2\mu^2 + \frac{3}{4\pi^2}\mu^4 - B, \quad (1)$$

$$e = \frac{19}{12}\pi^2 T^4 + \frac{9}{2}T^2\mu^2 + \frac{9}{4\pi^2}\mu^4 + B, \quad (2)$$

$$n = T^2\mu + \frac{1}{\pi^2}\mu^3, \quad (3)$$

which corresponds to the simple pressure-density relation

$$P = \frac{1}{3}(e - 4B). \quad (4)$$

The value of B is not known; however, some constraints can be derived. We can specify a lower limit of B due to the fact that nucleons do not decay spontaneously to two-flavor quark matter. Madsen [25] shows that this lower limit is $B^{1/4} \geq 145$ MeV and gives an expression for the energy per baryon E/A as function of B ,

$$E/A = 829 \text{ MeV} \frac{B^{1/4}}{145 \text{ MeV}}. \quad (5)$$

Since nuclear matter has an energy per baryon of $E/A \sim 930$ MeV, according to (5) bag constants lower than $B^{1/4} = 160$ MeV correspond to absolutely stable SQM.

The next step to a more realistic EoS would be to include the masses of the quarks. Although the current masses of u- and d-quarks are at most 10 MeV and are therefore negligible, the mass of the s-quark is of the order of 100 MeV. However, in this case an analytic expression for P , e and n is no longer possible for finite temperatures. Including quark masses as well as QCD interactions [26] leads, for example, at a given B to a the energy per baryon which is about 20 MeV higher than given by (5)[27] and thus shifts the range of bag constants in which SQM is absolute stable.

III. COMBUSTION

We model the conversion from hadronic matter into SQM as a combustion, initiated by a seeding of SQM which we assume to occur in the center of the star. We do not specify the origin of the initial SQM seed (see [5] for various possibilities, or [17] for new ideas). The flame front, initially consisting of the boundary surface of some central seed, propagates outwards and converts hadronic matter into SQM, provided this reaction is exothermic. If this is the case, the difference in the energy per baryon is released into internal energy and therefore the temperature increases. The analogous case in chemical combustion theory is called premixed combustion, where fuel and oxidizer are already mixed at low temperatures and the flame propagates by conduction of heat [28]. In the case of the burning of hadronic matter into SQM the abundance of s-quarks plays the role of temperature; accordingly the diffusion of s-quarks leads to the propagation of the flame front. The combustion process takes place on length scales of the micro-physical reactions, which can be estimated as follows: The disintegration of a nucleon into quarks happens on time scales of the strong interaction, $\sim 10^{-24}$ s, corresponding to a length scale of $\sim 10^{-13}$ cm. The conversion of a d-quark into an s-quark due to the weak interaction takes place in $\sim 10^{-8}$ s. Since the weak processes are much slower, they determine the time scale of the burning, leading to a width of the reaction zone, l_{burn} , not exceeding 10^2 cm, whereas realistic calculations yield $l_{\text{burn}} \sim 10$ cm [13]. These length scales are much smaller than the resolution we can achieve in our simulations ($l_{\text{resolved}} > 10^3$ cm) and therefore we cannot resolve the reaction zone. Instead, we model the conversion front as a discontinuity which separates the “unburnt” (hadronic) matter from the “burnt” (strange quark) matter and have to take the propagation velocity of the conversion front with respect to the fluid flow as an input parameter, since this velocity is not determined by the hydrodynamic equations but by micro-physical processes on scales of the internal structure of the conversion front.

A combustion can take place either as a supersonic detonation driven by a shock wave, or as a subsonic deflagration driven by diffusion processes. Since we cannot resolve the internal structure of the flame we have to decide before starting our computations whether to model the conversion as a deflagration or as a detonation. Drago et al. [12] examine the conversion of hadronic matter into quark matter based on the hydrodynamic jump conditions. They assume the combustion to start as a deflagration and conclude that the process should stay subsonic. Also Niebergal et al. [13] and Horvath [16] assume the conversion to be subsonic. Based on these recent publications we decided to choose a deflagration as combustion mode, though we do not exclude the detonation mode and might consider it in future work.

The relevant input velocity for a deflagration is the laminar burning velocity v_{lam} , which is only very poorly

known for the burning of hadronic matter into SQM. The first attempts to determine it were made by Olinto [14], who estimates v_{lam} based on the diffusion of strange quarks and the equilibration of the SQM via weak interactions. The resulting velocities are generally rather low but strongly temperature dependent and would lead to a wide range of neutron star conversion timescales from milliseconds up to several minutes. Recently, Niebergal et al. [13] conducted one-dimensional hydrodynamic simulations of the combustion flame, including neutrino emission and strange quark diffusion. They found laminar burning velocities much higher than in earlier work. Because the methods of Niebergal et al. [13] are more sophisticated than in previous publications, we adopt a weakly density-dependent laminar burning velocity based on a linear fit to their results. This leads to $v_{\text{lam}} \sim 10^8$ cm/s in the center of the initial neutron star at densities of $\epsilon \sim 10^{15}$ g/cm³. Since according to our simulations the burning velocity is strongly enhanced by turbulence, the importance to know the exact value of v_{lam} is rather subordinate (see below).

A. Turbulent Combustion

Under certain conditions the laminar propagation of the conversion front can be distorted by Rayleigh-Taylor (buoyancy) instabilities [see 29, and references therein]. A necessary condition for this is that the gradient of the gravitational potential and the gradient of the total energy density point in opposite directions (“inverse density stratification”).

In chemical flames, as well as during the thermonuclear burning of carbon and oxygen in the center of a white dwarf, the large amount of energy released during the burning process leads to a sharp increase in temperature. In chemical flames a strong increase of pressure, or a strong decrease in density at constant pressure, is the natural result and therefore is usually taken for granted in qualitative considerations. Similarly, in SNe Ia the degeneracy of the matter is partially lifted, therefore the density decreases also in this case, albeit not as strongly as in chemical flames. Moreover, in these cases, although the chemical abundances change during the burning process, the EoS does not change dramatically. In the case of the burning in white dwarfs at densities $\lesssim 7 - 8 \times 10^9$ g/cm³ this leads to an inverse density stratification, instabilities and turbulence [29]. However, because of the strongly degenerate state of matter in neutron stars and the fundamentally different EoS before and after the conversion process it cannot be taken for granted that the neutron star matter behaves in the same way as described above. The state of the fluid behind the conversion front is determined by the change of the EoS and the hydrodynamic jump conditions [see e.g. 12] which result from the conservation of the baryon flux density and the energy-momentum tensor across the flame surface and has to be computed in hydrodynamic

simulations. To explore if in the vicinity of the propagation front the density of the SQM is lower than the density of the hadronic phase for our choice of EoS is therefore one aim of this work.

The Rayleigh-Taylor instability can only grow and lead to turbulent motion if the perturbations of the front exceed some minimal length scale, λ_{\min} , which depends on the burning velocity, the gravitational acceleration g , and the density contrast between the total energy density of the hadronic phase e_h and the total energy density of the quark phase e_q [29],

$$\lambda_{\min} = 2\pi v_{\text{lam}}^2 \left(g \frac{e_h - e_q}{e_h + e_q} \right)^{-1}. \quad (6)$$

We calculate λ_{\min} for different setups in Section V A.

In the established heuristic turbulence model [30, 31] instabilities like the Rayleigh-Taylor instability (and secondary shear instabilities) lead to turbulent eddies on large scales, which decay successively into ever smaller eddies until, at the Kolmogorov length scale l_K , viscosity effects dissipate the smallest eddies into thermal energy. In this *turbulent cascade* kinetic energy is transported from the largest to the smallest scales and is finally dissipated. This picture assumes that magnetic fields do not significantly affect the dynamics. For the velocity fluctuation $v(l)$ on a given scale l , which can be interpreted as the turnover velocity of an eddy of size l , this model yields the *Kolmogorov scaling* [32],

$$v(l) = v(L) \left(\frac{l}{L} \right)^{1/3}, \quad (7)$$

where L is the integral scale, the size of the largest eddies.

The Reynolds number Re on different scales is therefore

$$Re(l) = Re(L) \left(\frac{l}{L} \right)^{4/3}, \quad (8)$$

since $Re(l) \propto v(l)l$. Horvath and Benvenuto [6] estimate the Reynolds number of flows in both neutron and strange stars to be $Re(L) \sim 10^{10}$. At the Kolmogorov scale $Re(l_K) \sim 1$ holds, so we get

$$l_K = L \left(\frac{Re(l_K)}{Re(L)} \right)^{3/4} \sim 10^{-8} \text{ cm}, \quad (9)$$

and hence $l_K \ll l_{\text{burn}}$.

The scale on which the eddy turnover velocity is equal to the laminar burning velocity is defined as the Gibson scale l_G [e.g. 28],

$$v(l_G) = v_{\text{lam}}. \quad (10)$$

Turbulence cannot distort the flame front on scales smaller than l_G since according to (7) on these scales the eddy turnover velocity is smaller than the laminar burning velocity, whereas on scales larger than l_G , the turbulent eddies alter the shape of the flame front.

If we assume the above scaling law for a rising Rayleigh-Taylor unstable bubble of typical size $L \approx 10^5 \text{ cm}$ and typical macroscopic velocity variations $v(L) \approx 10^9 \text{ cm/s}$, we find $l_G = 10^2 \text{ cm}$. The combustion theory was developed for chemical flames and only adapted to SNe Ia [33, 34], whereas no detailed studies were conducted for the case treated in this work. However, the Kolmogorov scaling was found to fit quite well in the case of SNe Ia [35, 36], so based on these results and in the absence of exact calculations we assume that this is the case for our problem as well and obtain

$$l_{\text{burn}} < l_G < l_{\text{resolved}}. \quad (11)$$

This leads to two important consequences: $l_{\text{burn}} < l_G$ means that the turbulent eddies cannot disturb the flame front. Thus, it can still be described as a well-defined discontinuity. The burning is said to take place in the *flamelet regime* [28]: Although the internal flame structure is not disturbed, the total burning rate is enhanced as turbulence alters the geometry and thus enlarges the surface of the front. Since $l_G < l_{\text{resolved}}$ the surface of the flame front is also enhanced on unresolved scales, leading to an increase in the effective front propagation velocity on these scales. This effective velocity is described by the *turbulent burning velocity* v_{turb} , which is defined as the mean propagation velocity of the flame front at the marginally resolved scale.

For strong turbulence, the turbulent burning velocity becomes independent of the laminar burning velocity, as is the case during the thermonuclear burning of a white dwarf. In this work we aim to explore if the same is true in the conversion process of a neutron star.

B. Conditions for Exothermic Combustion

Since we describe the conversion of hadronic matter into SQM as a combustion, and a combustion has to be, by definition, exothermic [37], we can specify the following necessary condition for the conversion to take place: The total energy density of the quark phase e_q in a thermodynamic state (P, X) has to be lower than the energy for the hadronic matter e_h in the same state [37],

$$e_h(P, X) > e_q(P, X), \quad (12)$$

where P is the pressure, X is the generalized volume, $X = (e + P)/n_B^2$, and n_B is the baryon density. In the case of our analytic EoS for SQM (4), this can be rewritten as a simple condition for the energy density of the hadronic phase [9, 38] :

$$e_h(P) > 3P + 4B. \quad (13)$$

From this relation it becomes clear that for each given total energy density e_h and temperature T_h the corresponding pressure of the hadronic phase P and the value of B determine whether the conversion can proceed in form of a combustion wave. Thus, after choosing the

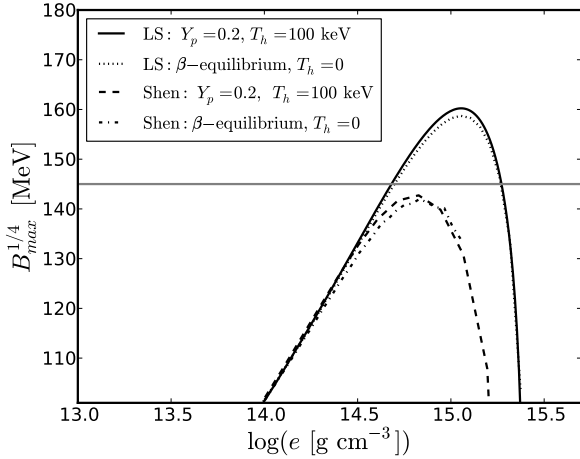


FIG. 1. Maximum bag constant B allowing an exothermic combustion as function of the total energy density e for two different hadronic EoS (Lattimer-Swesty with $K = 180$ MeV and Shen). The horizontal line indicates the theoretical lower limit of B . For each EoS, two cases are plotted: in the first case temperature T_h and proton fraction Y_p are kept constant, in the second case the matter is in β -equilibrium at zero temperature.

EoS and assuming a fixed T_h we can calculate for each e_h a critical bag constant, $B_{\text{crit}}(e_h)$, which is the largest possible bag constant for an exothermic combustion. The results of these calculations using both the LS EoS with $K = 180$ MeV and the Shen EoS are shown in Figure 1. Here the results are plotted for two different cases: In the first case we assume a constant temperature of the unburnt hadronic matter of $T_h = 100$ keV and a constant proton fraction of $Y_p = 0.2$. We adopt these assumptions for our numerical simulations presented in Section III. In the second case we assume β -equilibrium and zero temperature. As visible in Figure 1, the differences between the two cases are rather small and thus negligible for the qualitative treatment in this work. Also apparent from this figure is that for bag constants larger than the theoretical lower limit, $B^{1/4} > 145$ MeV, and temperatures found in the interior of cold neutron stars, hadronic matter described by the Shen EoS cannot be burned into SQM in an exothermic combustion, regardless of the density. In contrast, matter described by the LS EoS can be converted into SQM in an exothermic way at densities occurring in the center of neutron stars. The difference between the two hadronic EoS can be explained as follows. The Shen EoS is rather stiff, much stiffer than the LS EoS, that is at the same density the pressure is much higher. According to (13) this leads to a higher energy threshold for a given density. Based on this results we have to refrain from using the Shen EoS in our hydrodynamic simulations.

The LS EoS can be used with different incompressibility moduli K , we consider $K = 180$ MeV and $K =$

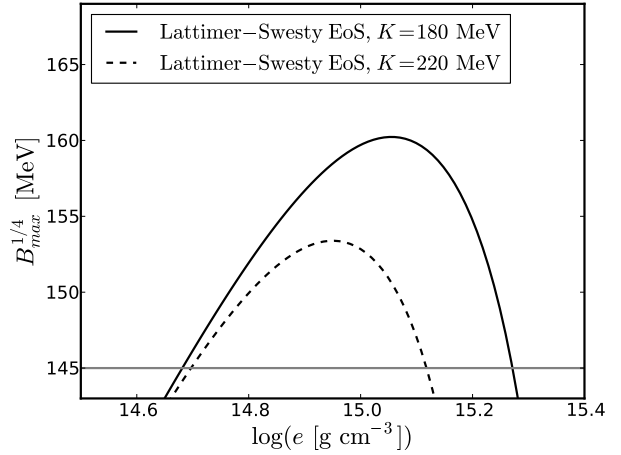


FIG. 2. Maximum bag constant B allowing an exothermic combustion as function of the total energy density e for the LS EoS and two different incompressibility moduli K . The horizontal line indicates the theoretical lower limit of B .

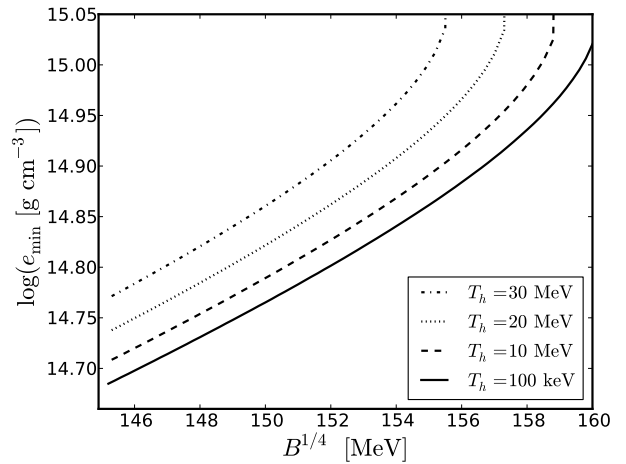


FIG. 3. Minimum total energy density e for an exothermic combustion as function of the bag constant B and for different temperatures T_h , using the Lattimer-Swesty EoS with $K = 180$ MeV.

220 MeV. We compare these two possibilities in Figure 2. For low bag constants ($B^{1/4} \sim 145$ MeV) the higher stiffness of the EoS with higher K affects the lower density limit only slightly, but for $B^{1/4} \gtrsim 152$ MeV the range in which exothermic combustion is possible becomes very narrow. Since our goal is to conduct simulations with higher bag constants to be able to compare the results for a wide range in the amount of released energy, we use in our simulations only the LS EoS with $K = 180$ MeV. In Figure 3 we concentrate on this case. Here we plot the minimum total energy density of the hadronic phase, $e_{\text{min}}(B)$, as a function of B and for different fixed temperatures. Since below this density threshold no combus-

tion is possible, it plays an important role in our simulations. The continuous line in Figure 3 shows the case with $T_h = 100$ keV, the temperature we adopt for the cold neutron star in our simulations. In addition we explore the effects of several higher temperatures. For temperatures up to $T_h = 1$ MeV only slight differences would be visible due to the strong degeneracy of the matter. In proto-neutron stars considerably higher temperatures occur, therefore also results for $T_h = 10, 20$ and 30 MeV are shown in the figure. These temperatures have a noticeable effect on the density threshold, as visible in Figure 3. In general, higher temperatures move the density threshold to higher densities.

IV. NUMERICAL METHOD

Taking advantage of the methodical similarities of combustion in white dwarfs and in neutron stars, we use an existing code, which is well tested and frequently applied for various SN Ia related simulations [e.g. 39, 40] and adapt it for the subject of this work. The main features of this code will now be described briefly.

The reactive Euler equations are solved using an explicit piecewise parabolic method (PPM) [41], a higher-order Godunov scheme. Specifically, our code is based on the PROMETHEUS implementation [42] of PPM.

To track the flame front we use the level-set method which was introduced by Osher and Sethian [43] and implemented in the code by Reinecke et al. [44]. In this scheme, a signed distance function G , which is positive in the burnt material and negative in the unburnt material, is assigned to each point in the computational domain. The zero level-set of G thus separates the burnt from the unburnt matter and marks the location of the flame front. The level-set is propagated with the burning velocity perpendicular to the flame surface and advected as a passive scalar without fundamental modifications of the hydrodynamics solver. It is now possible to calculate the burnt and unburnt volume fractions in each cell.

To ensure that the regions of highest interest are optimally resolved for a given fixed number of grid cells and no computational resources are wasted on regions of subordinate importance, the computational domain is separated into two grids [45, 46], an outer coarser grid, where the cell size increases outwards, and an uniformly spaced moving inner grid tracking the conversion front and expanding with it into the outer grid. This way we achieve an initial resolution in the center of the star of $\sim 2.6 \times 10^3 \text{ cm} \times (\text{grid cells per dimension}/128)^{-1}$, if our grid covers one octant of the star.

As described in Section III A, we cannot resolve the turbulent motion down to the Gibson scale. Therefore, we perform “large eddy simulations”: Only the largest scales of the system are resolved, while the turbulent motion on smaller scales is modeled by a subgrid scale (SGS) model. The SGS model determines the turbulent energy, from which the turbulent burning velocity can

be inferred. Schmidt et al. [47, 48] introduced a sophisticated localised SGS turbulence model and implemented it into the code. This model determines the SGS turbulence velocity q_{SGS} . The turbulent burning velocity v_{turb} is then obtained by setting [48]

$$v_{\text{turb}} = v_{\text{lam}} \sqrt{1 + \frac{4}{3} \left(\frac{q_{\text{SGS}}}{v_{\text{lam}}} \right)^2}, \quad (14)$$

with the laminar burning velocity v_{lam} as a lower limit.

The code as described was written to set up a white dwarf in a Newtonian gravitational potential and to model the thermonuclear burning of carbon and oxygen. Thus, it had to be adapted to the subject of this work. In contrast to the case of white dwarfs (compactness $(GM/Rc^2)_{\text{WD}} \sim 0.001$), in neutron stars (compactness $(GM/Rc^2)_{\text{NS}} \sim 0.1$) general relativistic effects cannot be neglected. Computations in full general relativity are, however, beyond our scope. Given the overall uncertainties, particularly in the EoS, we consider the error introduced by the use of Newtonian dynamics to be not critical, however a comparison of our results with general relativistic simulations would be interesting. But a modification of the gravitational potential cannot be avoided, otherwise the results would be completely beside the point. For example for a given mass of the neutron star the central density would be much lower and thus exothermic combustion would not be possible at all. Therefore an effective relativistic gravitational potential [49] based on the Tolman-Oppenheimer-Volkov (TOV) equations was implemented.

Further adaptations of the code to the new setup include the EoS for hadronic and quark matter as described in Section II, and, as a replacement for the “burning routine” in the original code, a routine which takes care of the conversion of the hadronic matter into SQM. This takes place by switching to the quark EoS and releasing the difference in the energy per baryon into internal energy, while conserving the total energy.

We set up one octant of the neutron star on a three-dimensional Cartesian grid with 128 or 192 grid cells in each dimension and applied reflecting boundary conditions at all borders of the computational domain. Burning is initialized in the following way: At the center of the star we construct a small sphere with a radius of $r_{\text{seed}} = 10^5 \text{ cm}$ on which a sinusoidal perturbation with an amplitude of $2 \times 10^4 \text{ cm}$ is superimposed. The initial seed is shown in the close-up of Figure 8 (a). When starting the simulation, the matter inside this small volume is converted instantly and constitutes the initial SQM seed.

Since both the size and the form of the initial seed are not known, we choose this configuration for numerical reasons: The size of the perturbations is similar to the minimum length scale for turbulent burning λ_{min} (cf. Sections III A and V A), therefore the front is expected to develop Rayleigh-Taylor instabilities soon after the start of the simulations. Smaller initial perturbations would need some time to grow before Rayleigh-Taylor instabili-

Model	Resolution	$B^{1/4}/\text{MeV}$	$M_{\text{unburnt}}/M_{\odot}$
B147_128	128^3	147	0.48
B150_128	128^3	150	0.66
B150_192	192^3	150	0.67
B152_128	128^3	152	0.77
B155_128	128^3	155	0.99

TABLE I. Overview of the different models. M_{unburnt} is the gravitational mass of the remaining hadronic outer layer at $t = 3.0$ ms, when the combustion can be considered as complete in all cases.

ties become possible. But since in the end the core is converted completely, the results should change only slightly, whereas the computational costs would be considerably higher. As described in Section III, we assume the combustion to be a deflagration and ignite the burning accordingly. Although we do not expect different initial configurations to alter our results considerably, possible effects of different initial geometries and different ways of ignition will be explored in future work.

V. SIMULATIONS

We conduct several runs with varying bag constant B . Since only some constraints on B are known, we can use it as a parameter to change the EoS for SQM and are thus able to control the amount of released energy from very high to rather low values, cf. (5). We vary B in a subset of the theoretically admissible range between a lower limit of $B_{\text{low}}^{1/4} = 147$ MeV and an upper limit of $B_{\text{high}}^{1/4} = 155$ MeV. At even higher B , the combustion would be restricted to the very innermost region of the neutron star or would not be possible at all, cf. Figure 1 and (12). We use $B^{1/4} > 155$ MeV only to test if instabilities grow at the beginning of the burning; results are presented in Section V A. In alternative units our chosen limits are roughly $B_{\text{low}} = 60$ MeV/fm³ and $B_{\text{high}} = 80$ MeV/fm³ – values also used as a lower and upper limits in the literature [e.g. 27].

We start our computations with a non-rotating, cold, isothermal “standard neutron star” in hydrostatic equilibrium, having an initial central total energy density of $e_c = 1.0 \times 10^{15}$ g/cm³, a gravitational mass of $M = 1.4 M_{\odot}$, a radius of $R = 11$ km, a proton fraction of $Y_p = 0.2$, and a temperature of $T = 100$ keV. We conducted four runs with a resolution of 128 grid cells per dimension and bag constants of $B^{1/4} = 147, 150, 152$ and 155 MeV, respectively. Table I shows an overview of the models presented here. In Figure 4 the temporal evolution of the conversion for different B is shown, represented by the gravitational mass of the remaining unburnt hadronic material.

In addition, we conducted one run with a higher resolution, 192 grid cells per dimension, using an intermediate

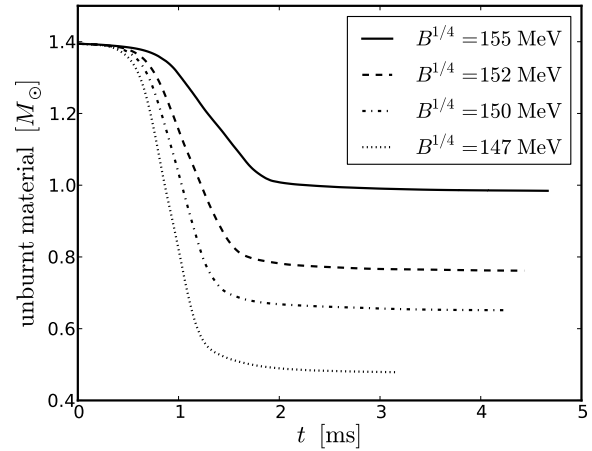


FIG. 4. Gravitational mass of unburnt (hadronic) material in the three-dimensional simulations for different bag constants B , as a function of time (models B155_128, B152_128, B150_128 and B147_128).

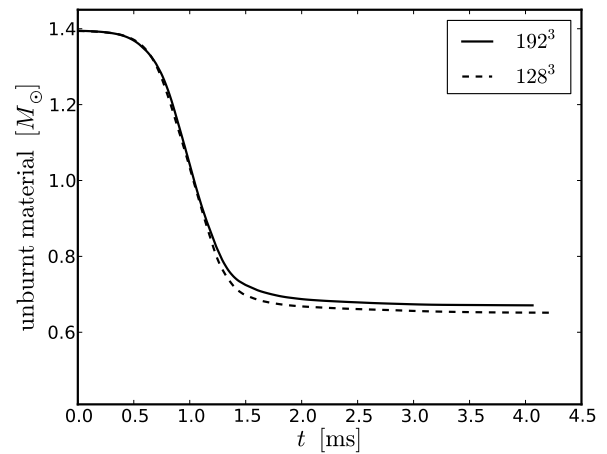


FIG. 5. Resolution study: Two models with $B^{1/4} = 150$ MeV which differ only in resolution (B150_192 and B150_128).

bag constant of $B^{1/4} = 150$ MeV (model B150_192). To study the effects of different resolutions, we compare in Figure 5 the two models B150_128 and B150_192, which differ only in the resolution (128^3 and 192^3 , respectively). Apparently there are only slight differences between the two models. In particular the slopes in the phase of rapid burning, which are determined by the conversion rate, which in turn depends on the turbulent burning velocity, agree very well. The different resolutions only become noticeable in the representation of the exact position of the density threshold for exothermic combustion – hence the slight discrepancy in the amount of unburnt matter at later times. Therefore we consider our simulations converged in the sense that the effects caused by resolution

$B^{1/4}/\text{MeV}$	145	147	150	152	155	157
At	0.11	0.091	0.067	0.051	0.027	0.010
$\lambda_{\min}/10^4 \text{ cm}$	3.6	4.4	6.2	8.5	16	45

TABLE II. Atwood number At and minimal length scale for turbulent burning λ_{\min} for different bag constants B at time $t = 0.1 \text{ ms}$, determined in three-dimensional simulations.

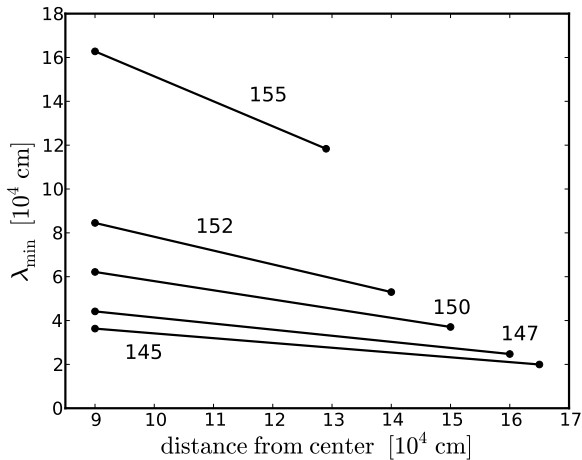


FIG. 6. Comparison of the minimal length scale for turbulent burning λ_{\min} in the early phase of the conversion process for different bag constants B and points in time, determined in three-dimensional simulations. The number on each line indicates $B^{1/4}$ in MeV. For each B the first and second point correspond to time $t_1 = 0.1 \text{ ms}$ and $t_2 = 0.2 \text{ ms}$, respectively. On the abscissa the average position of the conversion front at t_1 and t_2 is shown.

are smaller than uncertainties caused by other sources. Thus, we regard a resolution of 128 cells per dimension to be sufficient for our quantitative analysis.

After addressing the question of whether burning is turbulent, the results of the simulation with the highest resolution, model B150_192, are discussed in some detail below. In the subsequent sections we will briefly discuss differences in the two extreme cases (models B147_128 and B155_128).

A. Onset of Turbulence

We calculate the minimum length scale for turbulent burning, λ_{\min} , according to (6), see Section III A. To ensure comparability, we use the same three-dimensional setup for all B , as described above, and the same resolution of 128 grid cells in each dimension.

In Figure 6 we compare λ_{\min} at the beginning of the conversion process for different bag constants B and points in time. The density contrast is quantified by the Atwood number $At = (e_h - e_q)/(e_h + e_q)$. Table II lists At and λ_{\min} for different B . The values were de-

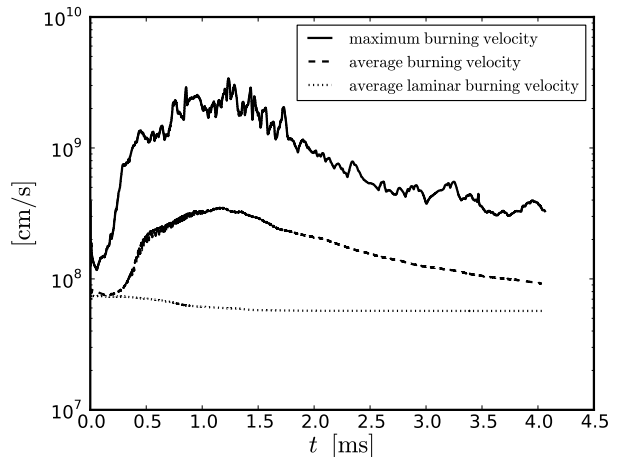


FIG. 7. Burning velocity: Comparison at each timestep of maximum burning velocity, average burning velocity and the underlying average laminar burning velocity. The averages were done over all cells in which burning occurs. Data from the high resolution run with $B^{1/4} = 150 \text{ MeV}$ (model B150_192).

termined at $t = 0.1 \text{ ms}$. As visible in Table II and Figure 6, λ_{\min} depends strongly on B , and becomes very large for high B . For the highest examined bag constant, $B^{1/4} = 157 \text{ MeV}$, λ_{\min} is comparable to the size of the system and no growth of Rayleigh-Taylor instabilities is expected. Bag constants starting at $B^{1/4} = 152 \text{ MeV}$ down to the lowest B , lead to smaller λ_{\min} which are comparable to or smaller than the size of the initial perturbations – thus instabilities can grow. In the simulation with $B^{1/4} = 155 \text{ MeV}$ this is not the case at $t = 0.1 \text{ ms}$ but already at some slightly later time, since λ_{\min} decreases with time as the gravitational acceleration becomes stronger, cf. (6) and Figure 6. Our simulations confirm this: in all runs except for $B^{1/4} \gtrsim 157 \text{ MeV}$ we see Rayleigh-Taylor instabilities form. Thus the burning of a neutron star into a quark star becomes turbulent in most cases, given our choice of EoS.

B. Intermediate Case: $B^{1/4} = 150 \text{ MeV}$

In this section we present a detailed discussion of the results of the simulation with a resolution of 192 grid cells per dimension and an intermediate bag constant, $B^{1/4} = 150 \text{ MeV}$ (model B150_192). According to (5) the energy per baryon in this case is $E/A = 858 \text{ MeV}$, corresponding to a difference of $\sim 70 \text{ MeV}$ per baryon with respect to the energy of nuclear matter.

In Figure 8 (a) the initial configuration including the SQM seed in the center can be seen. The shape of the seed as described in Section IV is shown additionally in the close-up in this figure. After ignition the conversion front propagates into the hadronic matter, at first in a

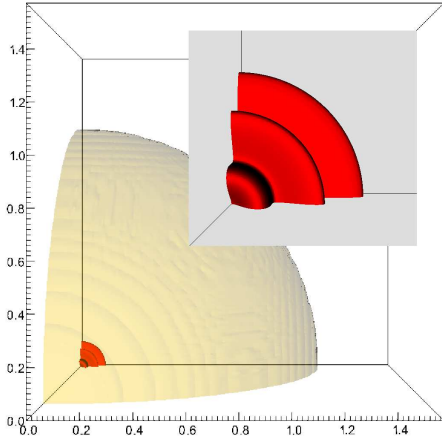
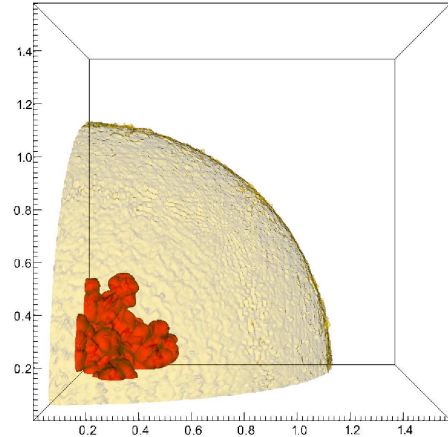
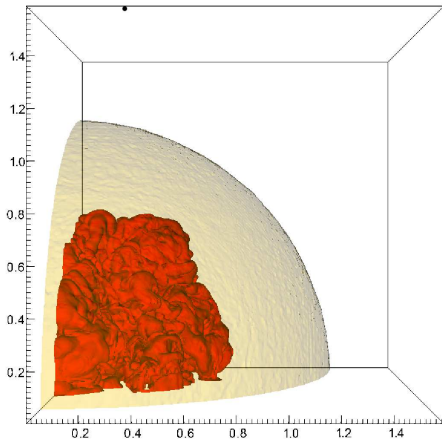
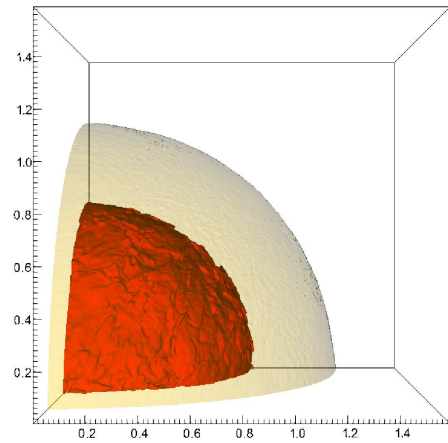
(a) $t = 0$ (b) $t = 0.7$ ms(c) $t = 1.2$ ms(d) $t = 4.0$ ms

FIG. 8. (color online) Model B150_192: Conversion front (red) and surface of the neutron star (yellow) at different times t . In (a) a close-up of the central region is added. Spatial units 10^6 cm.

laminar way until initial perturbations of the conversion front become unstable due to Rayleigh-Taylor instabilities. Until turbulence has fully developed, the conversion process stays in a short phase of nearly laminar burning while the instabilities grow, see Figure 4 which shows the amount of unburnt (hadronic) matter as a function of time, and Figure 7, where we compare the average laminar burning velocity, the average burning velocity and the maximum burning velocity at each timestep. The averaging was done over all cells in which burning occurs.

As the instabilities grow, typical mushroom-shaped

structures, rising plumes of SQM, are forming and hadronic matter is falling down in between. These structures can be seen in Figure 8 (b), where the conversion surface is shown at $t = 0.7$ ms. Starting at $t \sim 0.5$ ms strong turbulence develops and rapid burning takes place until $t \sim 1.5$ ms, as visible in Figure 4. The structure of the conversion front near the end of this phase of rapid burning can be seen in Figure 8 (c). The plumes grow until the conversion front reaches densities where the condition for exothermic combustion (12) is no longer fulfilled. They continue to grow laterally, until they eventually

merge, leaving bubbles of hadronic matter in between. Turbulence then weakens and the flame slows down. The remaining pockets filled with hadronic material shrink until they eventually vanish completely. Now all matter inside the volume confined by the above mentioned density threshold is burned and the star consists of an inner sphere of SQM containing about half of the mass and an outer layer of unburnt hadronic matter (cf. Figure 8 (d)). This outer layer has a mass of about $0.67 M_{\odot}$ and densities lower than the threshold (12) but mostly still super-nuclear (applying LS EoS and $B^{1/4} = 150$ MeV, the density threshold in cold matter is at about $1.8 \rho_{\text{nuclear}}$, see Figure 3).

Turbulent motions leads to burning velocities considerably higher than the laminar burning velocities, the maximum amplification factor is about 50 and on average between 2 and 20 (see Figure 7). This figure also clearly shows that the turbulent burning velocity and thus the strength of the turbulence increases rapidly until it reaches a maximum at $t \sim 1.0$ ms. At that point a steady but slower decrease starts. The maximum Mach numbers reached were about 0.2, i.e. the combustion was clearly subsonic. As we do not include any kind of cooling, the large amount of energy released in the burning process is turned into thermal energy and the inner SQM region is heated to temperatures of about 50 MeV in the center of the star.

We stopped this simulation at $t = 4.0$ ms. By then the conversion rate has dropped to a very low value and seems to approach zero asymptotically. Since at that time the system is approximately in hydrostatic equilibrium (the dynamical time scale of a neutron star is $\tau_{\text{dyn}} \sim 5 \times 10^{-2}$ ms) we do not expect any further conversion of a significant amount of mass. Therefore the structure of the remnant should not change if the simulation would have been carried on for longer timescales – at least in our model without cooling processes and in the approximation of a hydrodynamic combustion.

C. Lower Limit: $B_{\text{low}}^{1/4} = 147$ MeV

Now we briefly discuss the simulation with 128 grid cells per dimension and with our lower limit for the bag constant, $B_{\text{low}}^{1/4} = 147$ MeV (model B147_128). This corresponds to the largest difference in energy per baryon compared to nuclear matter, $E/A = 90$ MeV.

Qualitatively, the conversion process evolves in the same way as in the case described above (model B150_192), but there are some quantitative differences: The energy release is higher than in the intermediate case, therefore the burning leads to a stronger inverse density stratification, resulting in a faster growth of instabilities and stronger turbulence. The rising plumes of SQM are observable in Figure 9 (a) as typical “mushrooms”, like in the previous case. Comparing Figure 9 (a) and Figure 8 (b), both showing the conversion surface at $t = 0.7$ ms, clarifies that the conversion process takes

place considerably faster for the lower B . Figure 4 shows that after a short phase of slow burning, rapid burning occurs from $t \sim 0.4$ ms until $t \sim 1.5$ ms. Then the burning slows down and the conversion rate approaches zero. At $t = 5$ ms, the remnant has an inner SQM core with a radius of ~ 9 km, cf. Figure 9 (b), surrounded by an hadronic outer layer with a mass of $0.48 M_{\odot}$, the least massive outer layer in all our simulations. Central temperatures of the core reach 53 MeV, somewhat higher than in the previous case due to the higher energy release.

D. Upper Limit: $B_{\text{high}}^{1/4} = 155$ MeV

Finally we present the simulation with 128 grid cells per dimension and our highest bag constant, $B_{\text{high}}^{1/4} = 155$ MeV (model B155_128). Here the difference in energy per baryon, $E/A \sim 40$ MeV, is considerably lower than in the cases B147_128 and B150_128. Figures 10 (a) and 10 (b) show the conversion front at $t = 0.7$ ms and at the point when we stopped our simulation, at $t = 4.6$ ms. From the figures the similar evolution compared to the above described cases with lower B are visible. The lower E/A and the higher density threshold for exothermic burning (cf. Figure 3) lead to a slower and less violent burning, which ceases at higher densities compared to the models previously shown. Consequently, at the end of the simulation the resulting strange matter core is smaller and is surrounded by an hadronic outer layer of $0.98 M_{\odot}$. Temperatures of around 45 MeV are reached in the center. Figure 4 shows that the conversion rate, represented by the slope of the curves, is lower than in the other cases and the combustion takes longer although less material is burnt.

VI. CONCLUSIONS

We presented three-dimensional hydrodynamic simulations of the conversion of a neutron star into a quark star assuming different bag constants B for describing SQM. In all cases we observe growing Rayleigh-Taylor instabilities of the conversion front. The resulting turbulent motion enhances the conversion velocity strongly, leading to conversion timescales of $\tau_{\text{burn}} \sim 2$ ms for all B . However, recent suggestions [13, 16] that the turbulence enhances the burning speed to sonic or even supersonic velocities could not be confirmed, which came as no surprise since in the analogous case of SN Ia such a transition is not possible either as long as burning proceeds in the flamelet regime [33].

In all cases we observe at the end of our simulations a spherical SQM interior surrounded by an outer layer of hadronic matter. This outer layer exists because in our hydrodynamic approximation the combustion stops when the conversion front reaches conditions under which exothermic burning is no longer possible. Since this

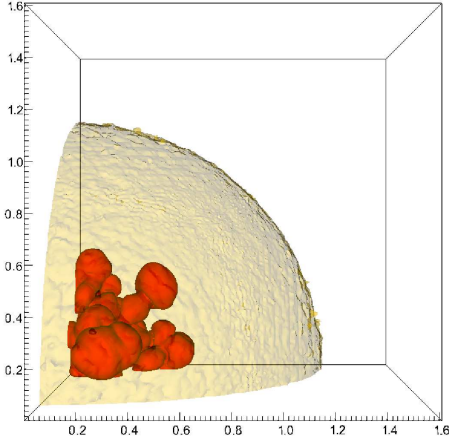
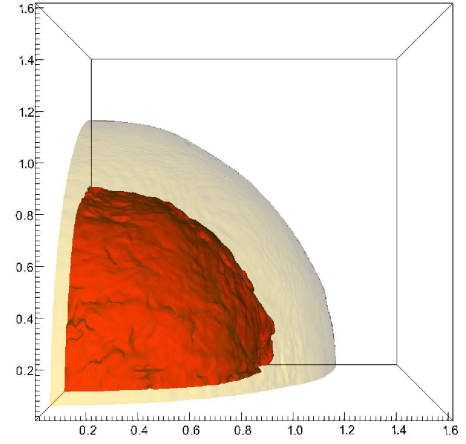
(a) $t = 0.7$ ms(b) $t = 3.1$ ms

FIG. 9. (color online) Model B147_128: Conversion front (red) and surface of the neutron star (yellow) at different times t . Spatial units 10^6 cm.

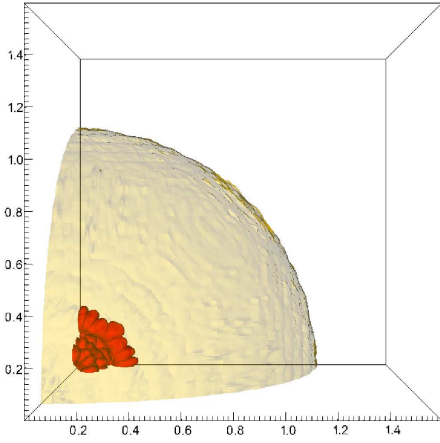
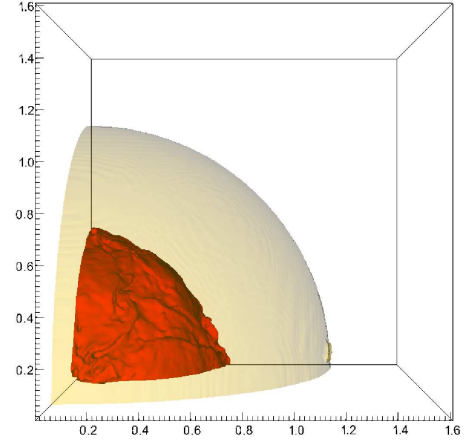
(a) $t = 0.7$ ms(b) $t = 4.6$ ms

FIG. 10. (color online) Model B155_128: Conversion front (red) and surface of the neutron star (yellow) at different times t . Spatial units 10^6 cm.

condition depends on density and is fulfilled for sufficiently high densities only, it can roughly be described as a density threshold which forms a boundary that separates the high density (burnt) strange quark matter and the low density (unburnt) hadronic matter. In our approximation we can make no statement on whether the conversion process proceeds further beyond this boundary by processes which cannot be described as a com-

bustion. Possibly free neutrons diffuse into the quark matter and are converted subsequently [14], a process that probably is exothermic, as Lugones et al. [9] already pointed out. Free neutrons are abundant in hadronic matter at densities higher than the neutron drip density, $e_{\text{drip}} \sim 4 \times 10^{11} \text{ g/cm}^3$. However we expect these additional processes to happen on much longer timescales than the combustion described in this work.

The obvious consequence of an at least temporary existence of an outer layer of unburnt hadronic matter is that the resulting quark star could support a rather thick crust, unlike bare strange stars, which can presumably support only a tiny crust. This would allow e.g. for pulsar glitches, if the timescale of the conversion after the combustion has ceased is large enough. Some authors suggested that the conversion of a neutron star into a strange star may eject neutron-rich material from the surface, and that in this ejecta the nucleosynthesis of heavy neutron-rich nuclei via the r-process may occur [50]. However, our results suggest that ejection of matter from the star is rather unlikely since the violent burning ceases before reaching the surface. Any subsequent continuation of the conversion by processes not describable by a combustion is expected to be much slower, and to take place in a much less violent way. But given our ignorance about these processes more detailed work on this subject may lead to differing conclusions.

The existence of the hadronic outer layers, or the possibility of exothermic combustion even in the center of neutron stars, depends (like many other properties) strongly on the EoS used for the hadronic as well as for the quark phase. Hence any firm prediction needs a more realistic treatment. Furthermore, the maximum mass configuration of non-rotating stars of both the LS EoS and our bag model EoS have $M_{\text{max}} < 2 M_{\odot}$ and therefore conflict with observations [22]. As mentioned before, we nevertheless use those EoS in this work because we consider them as sufficient for our first attempts. In future work we want to improve on this and plan to use more realistic EoS. Regarding the quark phase, finite strange quark masses and QCD-interactions can be included into the bag model. SQM bag model EoS which contain these corrections can support a $2 M_{\odot}$ neutron star, as was shown

by Weissenborn et al. [51]. Recently also the choice of micro-physical finite temperature EoS for nuclear matter has become larger [e.g. 52, 53], so we can consider additional hadronic EoS apart from the LS and Shen EoS which we used in this work. Another possibility is to consider the use of modern zero-temperature micro-physical EoS together with an ideal gas component to account for temperature effects, whose reliability has been tested in [54]. Further improvement would be achieved by adding neutrino cooling, which could be relevant since rather high temperatures are reached in the quark core. Until now we use an initial model resembling an old isolated neutron star, the same calculations could be done with a young (proto)neutron star and in connection with a core collapse supernova. Furthermore our computations should be extended to make statements about observable quantities. Therefore we plan to calculate the gravitational wave signal of the conversion of a neutron star into a quark star.

ACKNOWLEDGMENTS

The computations for this work have been carried out at the Rechenzentrum Garching of the Max Planck Society. We thank A. Bauswein, D. Blaschke, T. Fischer, G. Pagliara, M. Hempel, and J. Schaffner-Bielich for helpful discussions. This work was supported by CompStar, a Research Networking Programme of the European Science Foundation. The work of FR has been supported by Deutsche Forschungsgemeinschaft via the Transregional Collaborative Research Center TRR 33 “The Dark Universe”, the Excellence Cluster EXC153 “Origin and Structure of the Universe” and the Emmy Noether Program (RO 3676/1-1).

-
- [1] A. R. Bodmer, Phys. Rev. D **4**, 1601 (1971).
 - [2] N. Itoh, Progress of Theoretical Physics **44**, 291 (1970).
 - [3] E. Witten, Phys. Rev. D **30**, 272 (1984).
 - [4] P. Haensel, J. L. Zdunik, and R. Schaefer, A&A **160**, 121 (1986).
 - [5] C. Alcock, E. Farhi, and A. Olinto, ApJ **310**, 261 (1986).
 - [6] J. E. Horvath and O. G. Benvenuto, Physics Letters B **213**, 516 (1988).
 - [7] M. L. Olesen and J. Madsen, Nuclear Physics B Proceedings Supplements **24**, 170 (1991).
 - [8] H. T. Cho, K. Ng, and A. D. Spiliotopoulos, Physics Letters B **326**, 111 (1994), arXiv:astro-ph/9305006.
 - [9] G. Lugones, O. G. Benvenuto, and H. Vucetich, Phys. Rev. D **50**, 6100 (1994).
 - [10] G. Lugones and O. G. Benvenuto, Phys. Rev. D **52**, 1276 (1995).
 - [11] I. Tokareva and A. Nusser, Physics Letters B **639**, 232 (2006), arXiv:astro-ph/0502344.
 - [12] A. Drago, A. Lavagno, and I. Parenti, ApJ **659**, 1519 (2007), arXiv:astro-ph/0512652.
 - [13] B. Niebergal, R. Ouyed, and P. Jaikumar, Phys. Rev. C **82**, 062801 (2010), 1008.4806.
 - [14] A. V. Olinto, Physics Letters B **192**, 71 (1987).
 - [15] H. Heiselberg, G. Baym, and C. J. Pethick, Nuclear Physics B Proceedings Supplements **24**, 144 (1991).
 - [16] J. E. Horvath, International Journal of Modern Physics D **19**, 523 (2010), arXiv:astro-ph/0703233.
 - [17] M. A. Perez-Garcia, J. Silk, and J. R. Stone, Physical Review Letters **105**, 141101 (2010), 1007.1421.
 - [18] D. Leahy and R. Ouyed, MNRAS **387**, 1193 (2008), 0708.1787.
 - [19] R. Ouyed, M. Kostka, N. Koning, D. Leahy, and W. Steffen, ArXiv e-prints (2010), 1010.5530.
 - [20] J. M. Lattimer and F. D. Swesty, Nuclear Physics A **535**, 331 (1991).
 - [21] H. Shen, H. Toki, K. Oyamatsu, and K. Sumiyoshi, Progress of Theoretical Physics **100**, 1013 (1998), arXiv:nucl-th/9806095.
 - [22] P. B. Demorest, T. Pennucci, S. M. Ransom, M. S. E. Roberts, and J. W. T. Hessels, Nature **467**, 1081 (2010), 1010.5788.

- [23] J. Cleymans, R. V. Gavai, and E. Suhonen, *Phys. Rep.* **130**, 217 (1986).
- [24] A. Chodos, R. L. Jaffe, K. Johnson, C. B. Thorn, and V. F. Weisskopf, *Phys. Rev. D* **9**, 3471 (1974).
- [25] J. Madsen, in *Hadrons in Dense Matter and Hadrosynthesis*, edited by J. Cleymans, H. B. Geyer, & F. G. Scholtz (1999), vol. 516 of *Lecture Notes in Physics*, Berlin Springer Verlag, pp. 162–203, arXiv:astro-ph/9809032.
- [26] E. Farhi and R. L. Jaffe, *Phys. Rev. D* **30**, 2379 (1984).
- [27] A. Bauswein, R. Oechslin, and H. T. Janka, *Phys. Rev. D* **81**, 024012 (2010), 0910.5169.
- [28] N. Peters, *Turbulent Combustion* (Cambridge University Press, Cambridge, 2000).
- [29] F. X. Timmes and S. E. Woosley, *ApJ* **396**, 649 (1992).
- [30] L. F. Richardson, *Weather prediction by numerical process* (Cambridge University Press, Cambridge, 1922), republished Dover 1965.
- [31] A. N. Kolmogorov, *Dokl. Akad. Nauk SSSR* **30**, 299 (1941), in Russian.
- [32] L. D. Landau and E. M. Lifshitz, *Fluid Mechanics*, vol. 6 of *Course of Theoretical Physics* (Pergamon Press, Oxford, 1959).
- [33] J. C. Niemeyer and S. E. Woosley, *ApJ* **475**, 740 (1997), arXiv:astro-ph/9607032.
- [34] J. C. Niemeyer and A. R. Kerstein, *New Astronomy* **2**, 239 (1997).
- [35] F. Ciaraldi-Schoolmann, W. Schmidt, J. C. Niemeyer, F. K. Röpkke, and W. Hillebrandt, *ApJ* **696**, 1491 (2009), 0901.4254.
- [36] M. Zingale, S. E. Woosley, C. A. Rendleman, M. S. Day, and J. B. Bell, *ApJ* **632**, 1021 (2005), arXiv:astro-ph/0501655.
- [37] A. M. Anile, *Relativistic fluids and magneto-fluids: With applications in astrophysics and plasma physics* (Cambridge and New York, Cambridge University Press, 1989, 1989).
- [38] H. W. Barz, L. P. Csernai, B. Kampfer, and B. Lukács, *Phys. Rev. D* **32**, 115 (1985).
- [39] M. Reinecke, W. Hillebrandt, and J. C. Niemeyer, *A&A* **391**, 1167 (2002), arXiv:astro-ph/0206459.
- [40] F. K. Röpkke and W. Hillebrandt, *A&A* **431**, 635 (2005), arXiv:astro-ph/0409286.
- [41] P. Colella and P. R. Woodward, *Journal of Computational Physics* **54**, 174 (1984).
- [42] B. A. Fryxell, E. Müller, and W. D. Arnett, MPA Green Report 449, Max-Planck-Institut für Astrophysik, Garching (1989).
- [43] S. Osher and J. A. Sethian, *Journal of Computational Physics* **79**, 12 (1988).
- [44] M. Reinecke, W. Hillebrandt, J. C. Niemeyer, R. Klein, and A. Gröbl, *A&A* **347**, 724 (1999), arXiv:astro-ph/9812119.
- [45] F. K. Röpkke, *A&A* **432**, 969 (2005), arXiv:astro-ph/0408296.
- [46] F. K. Röpkke, W. Hillebrandt, J. C. Niemeyer, and S. E. Woosley, *A&A* **448**, 1 (2006), arXiv:astro-ph/0510474.
- [47] W. Schmidt, J. C. Niemeyer, and W. Hillebrandt, *A&A* **450**, 265 (2006), arXiv:astro-ph/0601499.
- [48] W. Schmidt, J. C. Niemeyer, W. Hillebrandt, and F. K. Röpkke, *A&A* **450**, 283 (2006), arXiv:astro-ph/0601500.
- [49] A. Marek, H. Dimmelfeier, H. Janka, E. Müller, and R. Buras, *A&A* **445**, 273 (2006), arXiv:astro-ph/0502161.
- [50] P. Jaikumar, B. S. Meyer, K. Otsuki, and R. Ouyed, *A&A* **471**, 227 (2007), arXiv:nucl-th/0610013.
- [51] S. Weissenborn, I. Sagert, G. Pagliara, M. Hempel, and J. Schaffner-Bielich, *ArXiv e-prints* (2011), 1102.2869.
- [52] M. Hempel and J. Schaffner-Bielich, *Nuclear Physics A* **837**, 210 (2010), 0911.4073.
- [53] S. Typel, G. Röpkke, T. Klähn, D. Blaschke, and H. H. Wolter, *Phys. Rev. C* **81**, 015803 (2010), 0908.2344.
- [54] A. Bauswein, H.-T. Janka, and R. Oechslin, *Phys. Rev. D* **82**, 084043 (2010).